Modeling Microstructure Development in Gray Cast Irons

DAVID D. GOETTSCH and JONATHAN A. DANTZIG

Recent years have seen increasing use of solidification process modeling as a tool to aid in the analysis and elimination of manufacturing defects in castings. Grain size and other microstructural features such as second-phase morphology and distribution are the primary factors in determining the mechanical properties in cast metals. In this work, a representation of nucleation and growth kinetics for gray cast irons, based on a statistical description of the microstructure, has been coupled with a commercial finite-element method code for transient heat-flow calculation to determine microstructure. Features predicted include eutectic cell size, fractions of gray and white iron, graphite morphology, percent pearlite, percent ferrite, and pearlite spacing. The predicted microstructure can then be used to determine the strength and fatigue properties using published correlations. The theoretical development and results of the finite-element–based model will be discussed and compared with experimental results.

I. INTRODUCTION

SOLIDIFICATION modeling has been used to aid in the location of feeding sprues, gates, runners, and risers, along with the orientation of the casting, and the selection of process variables such as pouring temperature and mold materials to eliminate porosity and cold shuts and to predict residual stresses.[1,2,3] While lack of integrity of the casting accounts for a significant percentage of scrap, failure to meet microstructural and mechanical specifications is also an expensive problem. As an aid to solving these types of problems, microstructure models that track the nucleation and growth of the microstructure in a solidification simulation have been developed.

One of the casting alloys which will benefit greatly from microstructure modeling is gray iron. The phases which will form during solidification are determined by the composition of the iron, the relative abundance of various nucleation sites, and how rapidly the metal is solidified. Cast irons may solidify in either the metastable Fe-Fe_3C system or the stable Fe-C system, or in both. The austenite matrix can transform to pearlite, ferrite, or both. This competition between phases complicates the modeling of microstructure development in these alloys. In Sections B–1 through B–4, the kinetics of formation of each of the different microstructures will be discussed in detail. However, we wish to discuss them in the context of inclusion in a macroscopic heat-transfer code, so this will be discussed first.

Macroscopic heat-flow modeling has become a well-studied subject, and we therefore confine our discussion to that necessary for understanding microstructural modeling. The transient heat-conduction equation is solved in the solidifying iron and in the mold, *viz.*

$$\rho \frac{dh}{dt} = \nabla \cdot (k \nabla T) \qquad [1]$$

where ρ is the density, h is the specific enthalpy, t is time, k is thermal conductivity, and T is the temperature. The enthalpy change may be written in terms of the sensible heat and the heat of transformation as

$$\frac{dh}{dt} = c_p \frac{dT}{dt} + L \frac{df}{dt} \qquad [2]$$

where c_p is the specific heat, L is the latent heat of the transformation, and f is the volume fraction transformed. In conventional macroscopic modeling, the specific enthalpy is assumed to be a known function of temperature, determined from a phase diagram or a solidification model. Thus, Eq. [2] may be rewritten as

$$\frac{dh}{dt} = \left(c_p + L \frac{df}{dT} \right) \frac{dT}{dt} = c_p^{\text{eff}} \frac{dT}{dt} \qquad [3]$$

Once appropriate boundary conditions are specified, Eq. [1] may be solved for the transient temperature field, typically using either a finite-difference or finite-element method.

When modeling microstructural development, however, the evolution of the transformation is dependent upon the transformation path, *i.e.*, f is not representable as a function of temperature alone. Instead, evolution equations are introduced to represent $f(t)$, based on kinetic models for nucleation and growth of the transformation product.

Coupling of the kinetics expressions with the equations describing macroscopic heat flow has been described by Oldfield,[4] Hellawell,[5] and in a series of recent articles by Rappaz,[6] Rappaz and Stefanescu,[7] and Stefanescu and Bandyopadhyay.[8] A distribution containing N spherical particles having a distribution of radii, each denoted by R, is introduced. The kinetic laws take the form of expressions for the nucleation rate, dN/dt, and the growth rate of (assumed) spherical particles, dR/dt. The latent heat of solidification can be incorporated into the macroscopic heat flow in various ways, using enhanced specific heat, heat sources, or combinations of these methods. One difficulty common to all of the implementations is tracking the evolution of the distribution of particle sizes during solidification.

In all of the numerical algorithms published to date,

DAVID D. GOETTSCH, formerly Research Assistant, University of Illinois, is Senior Project Engineer, GM Powertrain Division, General Motors Corporation, Casting Technology Center, Saginaw, MI 48605-50730. JONATHAN A. DANTZIG, Associate Professor, is with the Department of Mechanical and Industrial Engineering, University of Illinois, Urbana, IL 61801.

Manuscript submitted April 13, 1993.

the finite-difference method has been used for temporal discretization. This gives rise in a natural way to successive applications of the nucleation and growth laws at succeeding time-steps, first to introduce nuclei at early time-steps and then to follow their subsequent growth. The timescale for heat flow is typically much greater than for solidification kinetics, however, so that most researchers employ a two-level time-stepping scheme in which the macroscopic time-steps are used to determine overall heat flow from a control volume, Q_{ext}, after which the time-step is subdivided and reanalyzed to resolve the microstructure evolution. Although it has been successfully implemented, following individual particles (or small groups all having the same size) in the evolution of microstructure can lead to very inconvenient data structures and difficulties in error control.

Several investigators have attempted to skirt this problem by using a single cell radius in the microstructure model. Knowing the undercooling at time t, the grain density is updated by integrating the nucleation rate over the time interval, Δt. The average radius is then increased by integrating the growth-rate equation to obtain ΔR. The change in fraction solid for the spherical cells is then calculated using

$$\Delta f_s = f_s(t + \Delta t) - f_s(t) = 4\pi N \overline{R^2} \cdot \Delta R \cdot \psi \qquad [4]$$

Here ψ is a correction factor used to account for impingement of grains. (This factor will be discussed in more detail in Section III.) Finally, the variation of temperature between t and $(t + \Delta t)$ is recomputed so as to satisfy the heat balance:

$$\Delta T = \frac{1}{\rho c_p}\left(Q_{ext}\frac{S}{V}\Delta t + L\Delta f_s\right) \qquad [5]$$

where S is the surface area and V is the volume of the control volume. After updating the temperature, $T(t + \Delta t)$, the macroscopic calculation proceeds to the next time-step.

The method of tracking the cell density and the average cell radius is a simple and direct way to track the microstructure evolution. The problem with using this approach to describe the particle distribution is that it requires that

$$\bar{R} = \frac{1}{N_{tot}}\sum_{i=1}^{N_{tot}} R = \left(\frac{1}{N_{tot}}\sum_{i=1}^{N_{tot}} R^2\right)^{1/2} = \left(\frac{1}{N_{tot}}\sum_{i=1}^{N_{tot}} R^3\right)^{1/3} = R \qquad [6]$$

Unfortunately, there is no distribution for which Eq. [6] is valid, other than the trivial one in which all particles are the same size. Thus, there is no way of determining within the model the actual cell distribution or the error associated with using the average radius for the second and third moments of the distribution.

Further, most microstructure models do not report an algorithm for monitoring error or any convergence criteria for determining the size of the microscopic time-steps. The time-step size needed to resolve the nonlinear kinetic equations will depend on the state of solidification and the value of the empirical constants. The use of fine time-steps can expend considerable computing time unnecessarily, while using too large time-steps can introduce considerable error. What is needed is a better way to represent the microstructure characteristics and a robust method for solving the kinetic equations.

A. *Microstructure Model Using Statistical Description of Particle Distribution*

In this work, the distribution of particles which comprise the microstructure will be described by assuming that the radii fit into a generic distribution given by a polynomial, as shown in Figure 1. The kinetic equations are used to determine the parameters of the distribution which apply for each control volume. This allows us to model the physics of the nucleation and growth of a continuous cell distribution, yet reduces the variables needed to describe the microstructure to a manageable number. In addition, the statistical representation of the microstructure simplifies error control and data storage and provides a straightforward means for comparing the computed results with experimentally observed microstructures. It will be shown in Section III that the particular form of the distribution is not important for describing many microstructural features.

The volumetric density of eutectic cells whose size falls between particle radius ρ_c and $\rho_c + d\rho_c$ is denoted by $n(\rho_c) \cdot d\rho_c$. The distribution function, $n(\rho_c)$, is assumed to be quadratic in the particle radius, *i.e.*,

$$n(\rho_c) = a_0 + a_1\rho_c + a_2\rho_c^2 \qquad [7]$$

with the properties

$n(R) = 0$	the cell density at the maximum radius is zero.
$\left.\frac{dn}{d\rho_c}\right\|_{\rho_c=R} = 0$	the slope of the distribution at the maximum radius is zero.
$\int_r^R n(\rho_c)d\rho_c = N$	the total number of particles in the distribution is N.

With these assumptions, the constants $a_0 - a_2$ can be

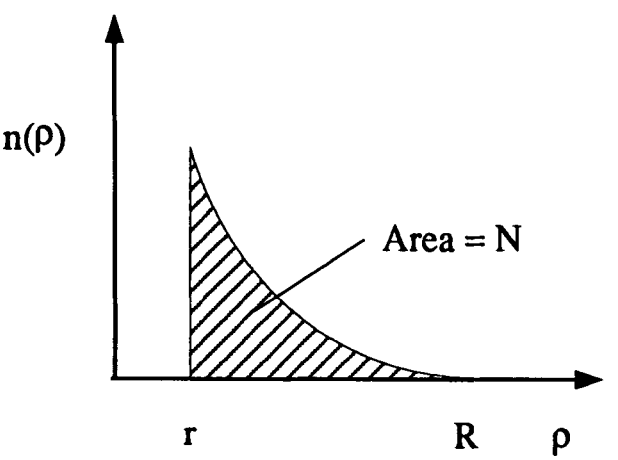

Fig. 1—Assumed cell distribution used in microstructure model.

evaluated in terms of the three parameters: total cell density, N, the minimum cell size, r, and the maximum size in the distribution, R:

$$n(\rho_c) = \frac{3N}{(R - r)^3}(R - \rho_c)^2 \quad [8]$$

The volume fraction of the solidified spherical cells is readily computed from the distribution as

$$f_s = \int_r^R \frac{4}{3}\pi\rho_c^3 \cdot n(\rho_c) \cdot d\rho_c$$

$$= \frac{N\pi}{15}(R^3 + 3R^2r + 6Rr^2 + 10r^3) \quad [9]$$

while the solidification rate is the time derivative of this expression:

$$\frac{df_s}{dt} = \Gamma \cdot \frac{dN}{dt} + \Theta \cdot \frac{dR}{dt} + \Phi \cdot \frac{dr}{dt} \quad [10]$$

where

$$\Gamma = \frac{\pi}{15}(R^3 + 3R^2r + 6Rr^2 + 10r^3)$$

$$\Theta = \frac{\pi N}{15}(3R^2r + 6Rr + 6r^2)$$

$$\Phi = \frac{\pi N}{15}(3R^2 + 12Rr + 30r^2) \quad [11]$$

Equation [10] assumes that the eutectic cells have a spherical shape throughout the entire growth process. This assumption is not valid at large solid fractions when cells impinge on one another.

A common method to account for impingement during growth is to multiply the solidification rate by an impingement factor, ψ. Johnson and Mehl[9] and Avrami[10] developed models for distributions of spheres where they allowed the spheres to grow without impediment, then corrected the volume fraction by a factor ψ to account for overlapping volumes. The volume of the spheres, which is no longer the true volume fraction, was called the extended volume, f_{ext}. The rate of volume change then took the form

$$\frac{df_s}{dt} = (1 - f_s) \cdot \frac{df_{ext}}{dt} \quad [12]$$

Price[11] and Rappaz[6] have calculated alternative impingement factors for uniformly sized spheres whose centers are placed at either the nodal points of a face-centered cubic (fcc) lattice, or a simple cubic lattice. The fcc and cubic impingement models begin to deviate from unimpeded growth at 74 and 52 pct solid fraction, respectively, whereas Eq. [12] applies from the beginning.

For our purposes, using Eq. [12] is inconvenient because the connection between the distribution and the true microstructure is lost when considering the extended volume. We can maintain the connection between the distribution and the volume if we instead assume that the growth rate of cells is slowed by the same factor ψ as a result of impingement. The physical interpretation of this form is that once impingement occurs, there is less surface area for growth, and that the "radius" of the particles (which are no longer spherical) may be represented as a sphere having the same volume. The two forms are not equivalent, however, and we will return to this point in Section III.

The evolution of the microstructure and the associated cell distribution over the different stages of solidification are shown schematically in Figure 2. When the volume is either entirely liquid, or only austenite has formed, no cells exist, and the cell density, N, is zero. Nucleation and growth take place once the temperature falls below the eutectic temperature, T_{eut}. During nucleation, all particles are introduced at the (specified) minimum size in the distribution, r. The existing cells grow, so that both the maximum radius, R, and the total cell density, N, increase, while the minimum radius, r, remains constant. At the point of recalescence, the nucleation of new particles ceases while the existing cells continue to grow. Thus, the cell density remains constant while all of the particles in the distribution are assumed to grow at the same rate, shifting the distribution to larger radii while maintaining its shape. When the fraction solid reaches unity, the evolution of the cell distribution is complete.

Each node in the finite-element mesh (which will be introduced in Section C) will have its own control volume and thus will have its own unique set of parameters for the distribution, fraction transformed, and temperature. The kinetic models introduced in Section B–1 through B–4 will yield expressions for dN/dt, dr/dt, and dR/dt. Determination of the temperature and microstructure distribution in a transient problem requires the solution of these kinetics equations, the transformation rate (Eq. [10]), and the following equation for the rate of temperature change:

$$\frac{dT}{dt} = \frac{\dot{Q}_{ext}}{\rho c_p} - \frac{L_f}{c_p}\frac{df_s}{dt} \quad [13]$$

where $\dot{Q}_{ext}$ is the rate of heat loss in the control volume computed during the macroscopic time-step. These relations form a system of five nonlinear ordinary differential equations for the microstructural parameters and temperature, with known values at the beginning of a time-step. We may readily solve this system of equations using standard algorithms, described in Section C. Note that we have effectively decoupled the transformation equations from the macroscopic heat-flow solution, and this can lead to errors if large time-steps are used in the macroscopic calculations.

B. *Phase Transformation Kinetics*

1. *Primary austenite dendrites*

Most commercial gray irons are hypoeutectic and therefore begin solidification by precipitation of primary austenite from the melt. Clyne and Kurz[12] studied the kinetics of austenite solidification and determined that because C diffuses very rapidly in Fe, and because nucleation of austenite is not difficult, the fraction of primary austenite solidified can be related to the temperature through the inverse lever rule, written as

$$f_{aus} = \frac{1}{1 - k'}\frac{T - T_L}{T - T_{\gamma 0}} \quad [14]$$

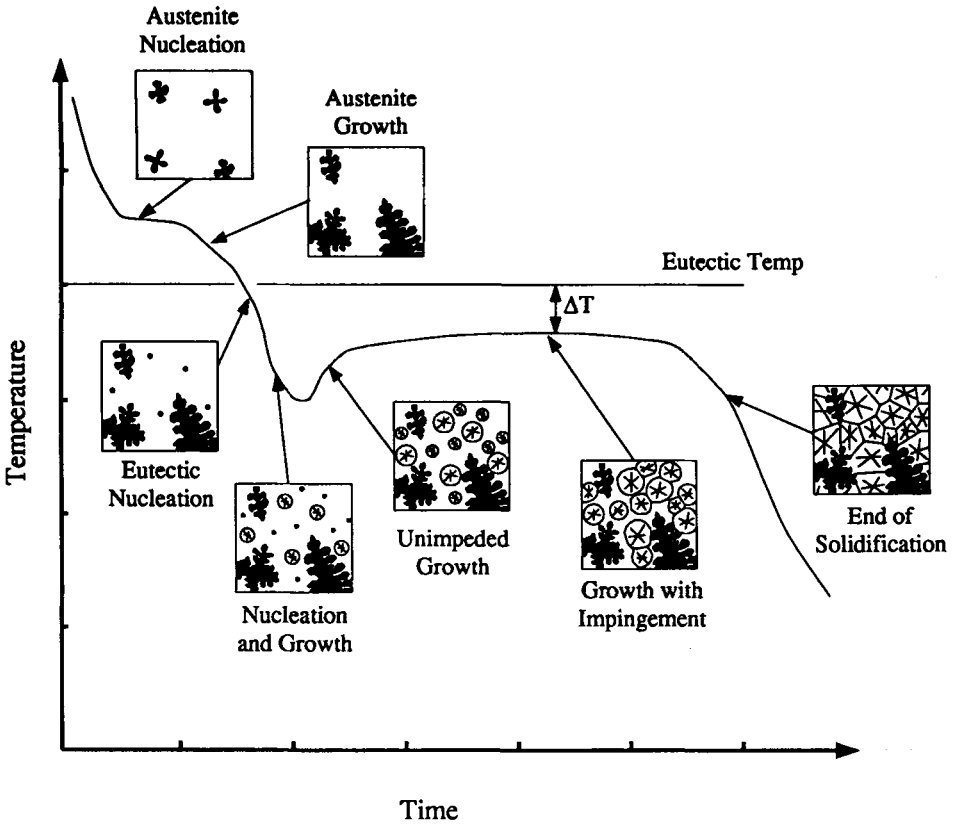

Fig. 2—Microstructure development in a gray iron of eutectic composition, along with the associated evolution of the eutectic cell size distribution.

where k' is the ratio of the slope of the liquidus curve to the slope of the solidus curve, $T_{\gamma 0}$ is the temperature at which the extrapolations of those curves intersect, and T_L is the liquidus temperature. Heine[13] provided the following detailed data for the solidus and liquidus curves for cast irons, treating them as pseudobinary sections through the Fe-C-Si ternary phase diagram:

$$T_L(°C) = 1569.0 - 97.3\ (\text{pct C} + 0.25\ \text{pct Si})$$

$$T_S(°C) = 1528.4 - 177.9\ (\text{pct C} + 0.18\ \text{pct Si})$$

$$T_{\gamma 0}(°C) = 1618.0 - 15.0332\ \text{pct Si}$$

$$\text{pct } C_{\text{eutectic}} = 4.26 - 0.3167\ \text{pct Si} \quad [15]$$

The austenite distribution coefficient may be calculated from the liquidus and solidus curves (Eq. [15]) as follows:

$$k = \frac{C_S}{C_L} = \frac{2.10 - 0.2165\ \text{pct Si}}{4.26 - 0.3167\ \text{pct Si}} \quad [16]$$

The evolution equations for primary austenite growth are then written as

$$\frac{df_{\text{aus}}}{dt} = \frac{df_{\text{aus}}}{dT} \cdot \frac{dT}{dt}$$

$$\frac{dT}{dt} = \frac{\dot{Q}}{\rho c_p - \rho L_{\text{aus}} \dfrac{df_{\text{aus}}}{dT}} \quad [17]$$

2. *Austenite-graphite eutectic cells*

The equation for the eutectic temperature determined by Glover *et al.*[14] correlated best with experimental results for the inoculated iron used in this study:

$$T_{\text{eut}}(°C) = 1135.06 + 13.89\ \text{pct Si} - 2.05\ \text{pct Si}^2 \quad [18]$$

Once this temperature is reached, nucleation of austenite-graphite eutectic cells can take place on or near the primary dendrites. Further nucleation may occur on distributed sites within the melt, and growth of existing nuclei ensues as more heat is extracted and the undercooling increases. Eventually, the latent heat released by solidification causes the temperature to rise (recalescence), after which nucleation ceases, and further solidification comes solely from growth of existing particles.

The basic theory of heterogeneous nucleation has been outlined by Turnbull and Fisher.[15] The theory predicts that the nucleation rate grows exponentially with undercooling, so that when a critical undercooling is reached, the time to saturation of all sites is less than 1 second. This short time suggests the further simplification of assuming that nucleation occurs instantaneously. However, it is usually observed that nucleation occurs over a longer time and a larger temperature range. This is commonly attributed to the existence of more than one type of nucleation site in the melt.

Gray iron eutectic nucleates on a variety of compounds, including graphite, ferrosilicon, calcium silicide, aluminum, oxides, and nitrides,[16] and each substrate should have its own characteristic nucleation temperature. Because of the complexity and uncertainty

of describing the exact amounts of the various nucleants in the melt, an empirical method was developed by Oldfield.[4] Using experimental data relating cell density to undercooling, Oldfield correlated the final eutectic cell density, N_{eut}, with the undercooling during freezing, ΔT, in the form

$$N_{eut} = A_e(\Delta T)^{n_e} \quad [19]$$

where $A_e = 7.12 \times 10^{-3}$ (nuclei/mm$^3 \cdot$ K^{n_e}) and $n_e = 2$ were determined experimentally. Differentiation yields an expression for the nucleation rate as follows:

$$\frac{dN_{eut}}{dt} = -n_e A_e(\Delta T)^{n_e - 1}\frac{dT}{dt} \quad [20]$$

Thorgrimsson *et al.*[17] studied the effect of the metal composition and inoculation practices on the nucleation of gray iron. He reported the following relation for the coefficients in Eq. [20]:

$$A_e = 10^{(-25+4.6 \cdot \text{CE}+4.06 \text{ pct inoculant})}$$

$$n_e = 12.56 - 2.15 \cdot \text{CE}$$

$$\text{CE} = \text{pct C} + \frac{1}{3}(\text{pct Si} + \text{pct P}) \quad [21]$$

where CE is the carbon equivalent. These values have been adopted for the results reported in Section II. Oldfield[4] and Magnin and Kurz[18] studied the growth kinetics in Fe-C eutectics. The growth rate was correlated with interfacial undercooling using an expression similar to Oldfield's nucleation rate equation. In terms of spherical particles of radius ρ_{eut}, the growth rate becomes

$$\frac{d\rho_{eut}}{dt} = B_e(\Delta T)^{m_e} \quad [22]$$

Oldfield reported values for B_e ranging from 2.5×10^{-5} to 34.5×10^{-5} (mm/s $\cdot$ K^{m_e}), and Magnin and Kurz gave a value of 38.7×10^{-6} (mm/s $\cdot$ K^{m_e}). Both groups reported $m_e = 2$. The latter work was also supported by theoretical analysis of solute redistribution near the interface. In this work, we perform experiments and modeling to determine B_e.

3. *Austenite-iron carbide eutectic*

Cast irons containing sufficient amounts of Si may solidify as either austenite-graphite eutectic during slow cooling, or as austenite-carbide eutectic by rapid cooling. The formation of carbide eutectic (often called white iron) is usually considered to be detrimental to a gray iron casting because of its high hardness and low toughness. The metallurgical mechanisms for formation of white iron were studied by Hillert and Subba Rao.[19]

Whether one obtains the gray or white form of cast iron is dependent on the nucleation potential and growth rates of the graphite and Fe_3C phases. Between the equilibrium graphite temperature and the Fe-Fe_3C eutectic temperature, only the graphite eutectic may nucleate and grow. Below the metastable eutectic temperature, however, the Fe-Fe_3C eutectic may also nucleate and grow. The Fe-Fe_3C formation temperature was given by Glover *et al.*[14] as

$$T_{carb}(°\text{C}) = 1138.2 - 6.93(2.5 \text{ pct C} + \text{Si}) - 1.717 (\text{pct Si} + 2.5 \text{ pct P})^2 \quad [23]$$

We assumed that the same nucleation law (Eq. [20]) applies to Fe-Fe_3C as applies to Fe-C eutectic. Hillert and Subba Rao[19] determined the growth kinetics for the Fe-Fe_3C eutectic to be

$$\frac{d\rho_{car}}{dt} = B_c \cdot (\Delta T)^{m_c} \quad [24]$$

where $B_c = 30 \times 10^{-3}$ (mm/sK^2) and $m_c = 2$ for cooperative growth of grey and white structures in cast iron. Note that B_c is about 10 times larger than B_e. For a separation between the eutectic temperatures of 10 K, then, the growth rates for the two phases become equal at less than 1 K below the metastable eutectic temperature. Thus, if this lower temperature is reached before solidification is complete, the remaining liquid will freeze as almost entirely white iron. When the temperature falls below the Fe-Fe_3C eutectic temperature, the Fe-C eutectic is assumed to stop growing, and the appropriate parameters in their kinetics equations are set to zero. In this formulation, we allow the Fe-Fe_3C eutectic to nucleate over the entire solidification range, so that white iron may also form after recalescence.

4. *Pearlite and ferrite grains*

After solidification is complete, further cooling reaches the eutectoid temperature, whereupon the austenite decomposes into pearlite or ferrite grains. Glover *et al.*[14] determined the equilibrium eutectoid temperature to be

$$T_{eud}(°\text{C}) = 723.0 + 22.7 \text{ pct Si} \quad [25]$$

The relative amounts of pearlite and ferrite are determined primarily by the chemical composition of the iron, the cooling rate during the decomposition of the austenite, and the nature of the graphite structure.[20] Experimental data for a 0.78 pct C, 0.63 pct Mg steel were presented by Mehl and Dube[21] and fitted to the following correlations for the nucleation and growth rate for pearlite cells:

$$\frac{dN_{perl}}{dt} = 5.07 \times 10^3 \left(\frac{\text{nuclei}}{\text{mm}^3 \cdot \text{s}}\right) \exp\left(\frac{-370 \text{ K}}{\Delta T_{eud}}\right)$$

$$\frac{d\rho_{perl}}{dt} = 0.168 \left(\frac{\text{mm}}{\text{s}}\right) \exp\left(\frac{-94.8 \text{ K}}{\Delta T_{eud}}\right) \quad [26]$$

where ΔT_{eud} is the undercooling below the eutectoid temperature, T_{eud}.

In modeling the development of ferrite grains, Stefanescu and Kanetkar[22] used a diffusion-controlled growth-rate equation:

$$\frac{d\rho_{ferr}}{dt} = \frac{C_2 - C_3}{C_4 - C_3}\left(\frac{D_c^\alpha}{R_\alpha^2\left(\frac{1}{R_\alpha} - \frac{1}{R_0^\alpha}\right)}\right) \quad [27]$$

where D_c^α is the diffusivity of C in ferrite, reported to be

9×10^{-7} cm^2/s, R_α is the radius of the ferrite grain, R_0^α is the radius of the ferrite nucleus, C_2 is the C content in the middle of the ferrite grain, C_3 is the C content at the ferrite-austenite interface, and C_4 is the C content in the austenite. Nucleation was assumed to be instantaneous, with the number of ferrite grains prespecified between 1.7×10^4 and 2.5×10^6 (grains/mm^2). We adopted this model in our work. Because the volumetric cell density is specified (from the austenite cell density), the minimum cell radius, r_{ferr} of the cell density distribution was allowed to grow from the onset of undercooling.

When modeling two competing transformations, such as pearlite *vs* ferrite or graphite eutectic *vs* Fe-Fe_3C, the addition of the second structure increases the number of ordinary differential equations for microstructural parameters from five to nine.

5. *Summary*

In view of the power law form for the kinetic relations of each transformation, we may write the evolution equations in a generic form. Table I summarizes the evolution equations for the microstructural distribution parameters and temperature during the various stages of the transformation process.

6. *Computational implementation*

The microstructure kinetics equations that have been discussed yield a series of simultaneous, nonlinear, ordinary differential equations with known initial values at the beginning of each macroscopic time-step. These equations are solved for each node in a finite-element mesh at which they apply by integration over the macroscopic time-step using the Bulirsch–Stoer method with adaptive step-size control.[23] The main algorithm is known as "Richardson's deferred approach to the limit." Adaptive step-size control allows the integration time-step size to be as large as possible, while still maintaining a specified truncation error. The error control parameter is defined as

$$\frac{Y^i_{err}}{Y^i_{scal}} \leq \varepsilon \qquad [28]$$

where Y^i is the ith dependent variable, ε is the local error tolerance, usually taken to be 1×10^{-3}, and the scaling factor is calculated from the relation

$$Y^i_{scal} = |Y^i| + \left| h \cdot \frac{dY^i}{dt} \right| \qquad [29]$$

where h is the microscopic time-step size. The reader is referred to Reference 23 for further details of the algorithm.

C. *Implementation of Microstructure Model*

The microstructure rate equations are coupled to the macroscopic heat-flow equations using the temperature-recovery method. This method consists of two parts in the calculation of the temperature field for each time-step. The first part uses the finite-element method to calculate the temperature field from the energy equation without including the latent heat generation. The rate of heat loss, $\dot{Q}$, at each node during the macroscopic time-step is computed as

$$\dot{Q} = \rho c_p(\text{constant}) \frac{\Delta T_{macro}}{\Delta t_{macro}} \qquad [30]$$

with the assumption that the specific heat is constant over the time-step. In the second part, the computed temperature field is then corrected, or "recovered," to the true solution by taking into account the release of the latent heat using Eq. [13]. A detailed analysis of the temperature-recovery method may be found in the work of Tszeng *et al.*[24]

The flowchart for the entire microstructure modeling part of the code is shown in Figure 3. The input to the driving routine MICRO at each time-step includes the nodal temperatures, the temperatures at the last time-step, the time and the size of the last time-step. At the first time-step of the simulation, the material composition, latent heat, and kinetic constants are read in from a data file. The equilibrium temperatures for all of the phase changes are calculated and stored, and nodes which are part of the melt (melt nodes) are determined.

The next step in the program is the updating or initialization of the microstructure variables for each melt node. After updating the variables, MICRO loops through all the melt nodes and calculates T, N, r, R, and f at time t from the initial conditions at time $(t - dt)$. Once a solution is determined at time t, the microstructure variables are stored, and the recovered temperatures replace the original temperature array.

The microstructure computation has been implemented within a commercial finite-element code, FIDAP.[25] Other codes could be used, provided that the capability to call external routines at the end of each macroscopic time-step, and to alter internal variables, such as temperature, is provided. The only changes to the standard version of the code are the addition of one

Table I. Kinetic Expressions Used under Various Conditions, Including Specification of When Condition Applies

Criteria → Quantity ↓	Untransformed $T > T_{trans}$	Nucleating $T < T_{trans}$ and $dT/dt < 0$	Growing After $dT/dt \geq 0$ $f_{trans} < 1$	Transformed $f_{trans} = 1$
dr/dt	0	0	$B(\Delta T)^m \cdot \psi$	0
dR/dt	0	$B(\Delta T)^m \cdot \psi$	$B(\Delta T)^m \cdot \psi$	0
dN/dt	0	$-n \cdot A(\Delta T)^{n-1}\, dT/dt$	0	0
df/dt	0	$\Gamma\, dN/dt + \Theta\, dR/dt$	$\Theta\, dR/dt + \Phi\, dr/dt$	0
dT/dt	$\dot{Q}/\rho c_p$	$\dot{Q}/\rho c_p - L/c_p \cdot df/dt$	$\dot{Q}/\rho c_p - L/c_p \cdot df/dt$	$\dot{Q}/\rho c_p$

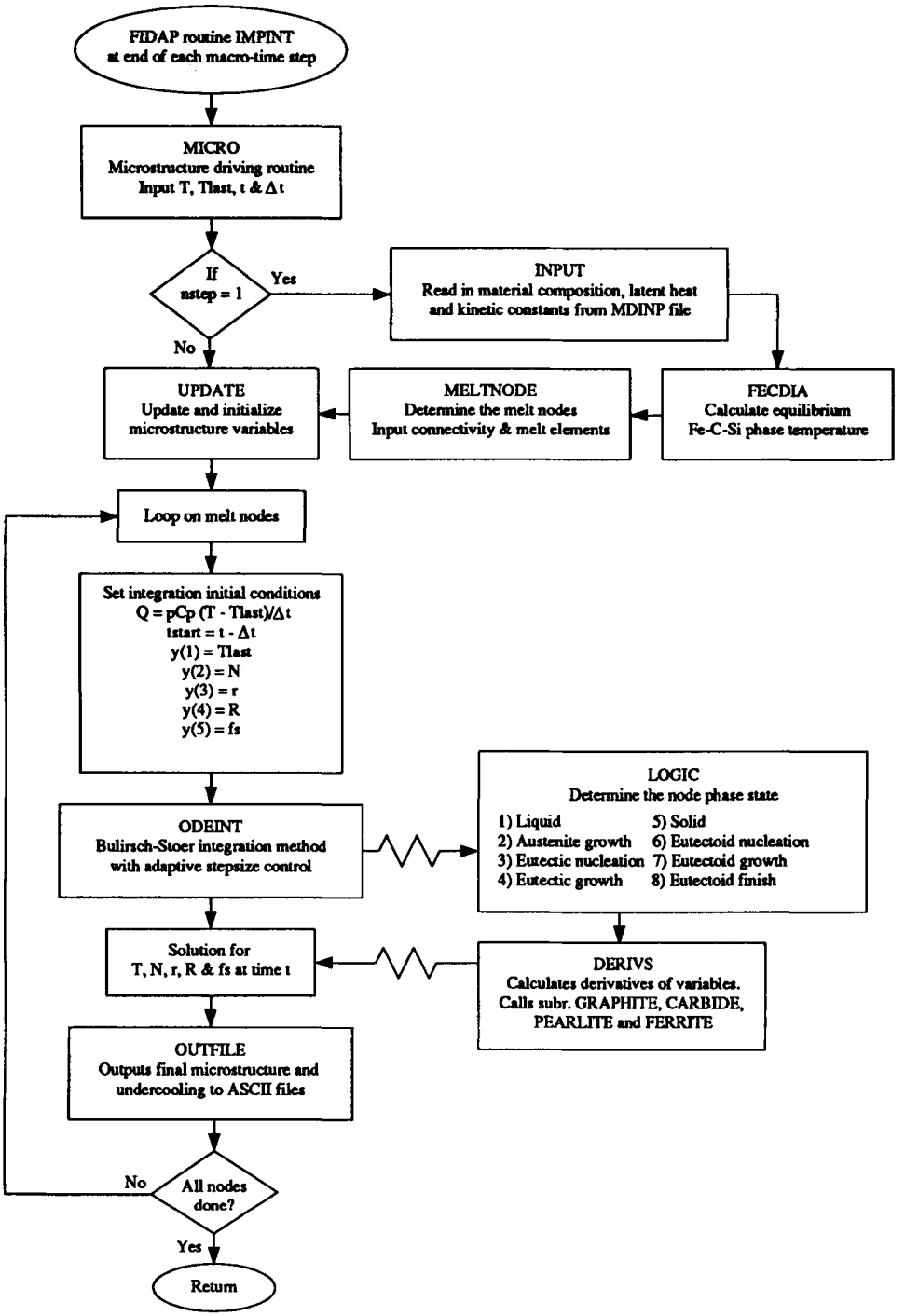

Fig. 3—Flowchart of microstructure model routines. Uppercase names refer to subroutine names.

subroutine call and a minor modification of the variable time-stepping algorithm, described in this section. The reader is referred to any of several finite-element method texts and Reference 25 for a detailed description of the finite-element method solution of transient heat-flow problems. The finite-element equations are solved using successive substitution to resolve the nonlinear algebraic equations for the nodal temperatures at each time-step. Convergence was typically declared when the root-mean-square error for both nodal temperatures and residual forces fell below 0.001.

Macroscopic time integration is performed using a backward Euler method in conjunction with a variable time-stepping algorithm. The size for the next time-step is chosen based on an estimate of the local truncation error derived from a predictor-corrector formulation of the transient problem. In the standard formulation in FIDAP, this error is estimated from the nodal temperatures as

$$\|d_{n+1}\|^2 = \frac{1}{N_T}\sum_{i=1}^{N_T}\frac{1}{4}\left[\frac{T^c_{n+1} - T^p_{n+1}}{|T_{n+1}|_i + T_{\max}}\right]^2 \qquad [31]$$

where $\|d_{n+1}\|$ is the norm of the error at time-step $n + 1$, i represents the node number, and the superscripts p and c refer to predictor and corrector, respectively.

Averaging of the errors over all of the nodes in the norm calculation in Eq. [31] can admit large local errors, particularly when the mesh is large. This is an endemic problem for solidification simulations, where the nodes undergoing solidification at any one time represent a small fraction of the entire mesh, but the largest source of errors. To control the local errors, a maximum nodal error is calculated using the form

$$(d_{n+1})^2_{\max} = \max_{\text{all } n} \frac{1}{4} \left[\frac{T^c_{n+1} - T^p_{n+1}}{|T_{n+1}|_i + T_{\max}} \right]^2 \quad [32]$$

The size of the next time-step is computed as

$$dt_{n+1} = dt_n \sqrt{\frac{\varepsilon}{D}} \quad [33]$$

where

$$D = \begin{cases} \|d_{n+1}\| & \text{when } (d_{n+1})_{\max} \le M \cdot \|d_{n+1}\| \\ (d_{n+1})_{\max} & \text{when } (d_{n+1})_{\max} > M \cdot \|d_{n+1}\| \end{cases} \quad [34]$$

where ε is a tolerance, usually taken to be 1×10^{-4}, dt_n is the time increment, and M is a specified value, typically 10. Stated in words, when the maximum nodal error exceeds the error norm by a factor M, the maximum nodal error is used in place of the error norm to determine the size of the next time-step.

II. EXPERIMENTAL METHODS AND RESULTS

The test castings shown in Figure 4 were made to evaluate the microstructure models. Six cylinders of different diameters (12.7, 15.2, 19.1, 25.4, 33.0, and 63.5 mm) were included to provide a range of cooling rates. The casting design was used by Oldfield[4,26,27] and Horsfall[28,29] in a series of articles investigating gray iron solidification. The cylinders are arrayed in a hexagonal pattern about a central sprue which feeds all of the castings from below. Air-bonded silica sand was used for the molds. A Type K thermocouple in a 4 × 5-mm oval alumina sleeve was embedded in the center of each cylinder, and temperatures were recorded at approximately half-second intervals.

Two castings were poured from separate heats, with the compositions shown in Table II. Both heats were inoculated with 0.3 wt pct of superseed (Sr-50 pct Si type), and the pouring temperatures were approximately 1475 °C and 1450 °C for castings 3-28-1 and 3-28-5, respectively. The twelve castings were sectioned and examined metallographically to determine the eutectic cell density, maximum graphite flake size, and percentage of each type of graphite. The results of the temperature and metallurgical measurements are shown in Tables III and IV. No evidence for the formation of white iron was found in these samples.

The specimens were polished using a 0.3-μm grit on a felt polishing wheel. Stead's reagent[30] was swabbed

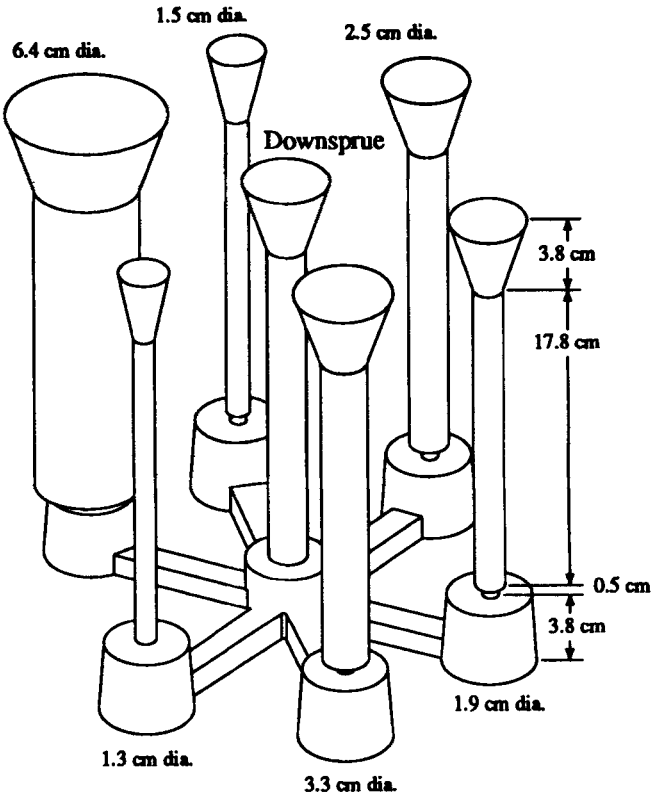

Fig. 4—Arrangement of test cylinders.[26]

onto dry specimens using a cotton ball. No increase in definition was found after 1 minute of etching time. The specimen was then rinsed with ethyl alcohol and hot-air dried.

A 35-mm camera with a flat-field lens was used to view and photograph the etched samples. The best resolution was obtained when the camera was set at a 20 deg angle to the specimen's face, illuminated by a diffuse light placed to the side. A series of circular stencils with known diameters were placed on the specimen face to provide a reference for cell counting. The diameter of the photograph was chosen so that there were at least 50 grains within the measurement area, except on the largest (63.5-mm diameter) casting, where the large cell sizes and limited depth of field limited us to using just 25 grains within the area. A count was made of the number of grains completely within the area, n_1, and the number of grains intersecting the perimeter of the test area, n_2. The number of grains per unit area was then computed using the formula

$$N_A = \frac{\left(n_1 + \frac{n_2}{2}\right)}{\text{measurement area}} \quad [35]$$

The volumetric density was determined using the stereological equivalence[31]

$$N_A = 1.169 \cdot N_V^{0.67} \quad [36]$$

Dawson and Oldfield[32] conducted a study of the scatter in cell measurement using line count, area count, and

Table II. Composition of Iron Used in Casting Trials at Caterpillar Mapleton Foundry

Casting	C	Si	Mn	P	S	Cr	Cu	Ni	Mo	Fe
3-28-1	3.25	2.08	0.60	0.02	0.07	0.16	0.48	0.13	0.29	balance
3-28-5	3.30	2.21	0.58	0.02	0.07	0.16	0.47	0.13	0.29	balance

Table III. Experimental Data from Casting 3-28-1 (3.25 Pct C, 2.08 Pct Si, and 3.94 Pct CE)

Casting Diameter (mm)	Maximum Eutectic Undercooling (°C)	Eutectic Cell Density		Maximum Graphite Flake Length (mm)	Percent Type D and E Graphite	Maximum Eutectoid Undercooling (°C)
		(cells/mm^3)	(cells/cm^2)			
12.7	NA	75	2080	0.110	50	NA
15.2	34	46	1490	0.127	40	121
19.1	21	24	980	0.163	18	98
25.4	19	12	600	0.218	8	84
33.0	15	4.9	340	0.364	3	NA
63.5	15	0.47	80	0.505	2	NA

NA = not available.

Table IV. Experimental Data from Casting 3-28-5 (3.30 Pct C, 2.21 Pct Si, and 4.04 Pct CE)

Casting Diameter (mm)	Maximum Eutectic Undercooling (°C)	Eutectic Cell Density		Maximum Graphite Flake Length (mm)	Percent Type D and E Graphite	Maximum Eutectoid Undercooling (°C)
		(cells/mm^3)	(cells/cm^2)			
12.7	NA	50	1600	0.137	22	127
15.2	34	44	1450	0.161	18	121
19.1	33	38	1350	0.157	10	96
25.4	20	14	690	0.277	10	85
33.0	16	8.3	480	0.296	8	NA
63.5	13	0.87	110	0.440	5	NA

NA = not available.

comparator methods for low- (0.034 pct), medium- (0.5 pct), and high-phosphorus (1.1 pct) irons. They found that higher phosphorus levels led to more diffuse grain boundaries. The iron used in this study had a low phosphorus content (approximately 0.02 pct). Of the three measurement methods, the area count had the lowest "uncertainty" index (20 pct) for low-phosphorus irons. This value was used to define the error bars which appear in Figures 5 and 10.

The same procedure outlined by Oldfield was used to determine the nucleation and growth coefficients for the test castings used in this study, as follows. Figure 5 shows a plot of the cell density *vs* the square of the maximum eutectic undercooling for castings 3-28-1 and 3-28-5. The small difference in composition and pouring temperature between the two castings did not make a significant difference in their measured cell densities. A nucleation coefficient of $A_e = 36.63 \times 10^{-3}$ (cells/mm$^3 \cdot$K^2) best describes the relationship between the density and undercooling for the two castings. This calculated nucleation constant was then used in a series of simulations with different growth constants to determine the value of B_e. A 25.4-mm-diameter casting was used as the base case. Using the results shown in Figure 6, the growth-rate constant which corresponded to the observed maximum undercooling, 17 °C, was selected as the correct value, yielding $B_e = 3.84 \times 10^{-5}$ (mm/s $\cdot$ k^2). Note that this value is very close to that reported by Magnin and Kurz.[18] A test of the validity of the model is how well these constants predict the microstructural features in the remainder of the castings.

The nucleation and growth coefficients thus determined were then used in a simulation considering all six castings. A horizontal slice through the center of the mold was made, to allow a two-dimensional simulation in the plane of the thermocouples to be performed. The mesh, illustrated in Figure 7, has 3948 elements and 3865 nodes. The thermal properties for the mold and gray iron are given in the Appendix.

Computed temperature histories for the castings in two molds are shown in comparison to experimental measurements in Figures 8 and 9. The equilibrium liquidus eutectic, and eutectoid temperatures for the composition in Table IV are 1211 °C, 1155 °C and 770 °C, respectively. The maximum recorded temperature for the largest casting was used as the initial condition for all of the castings in the simulation. Time "zero" was chosen for each experimental temperature curve to be the time when the temperature first exceeded 100 °C. The predicted results compare well with the experimental data. The lack of a defined recalescence in the experimental data shown

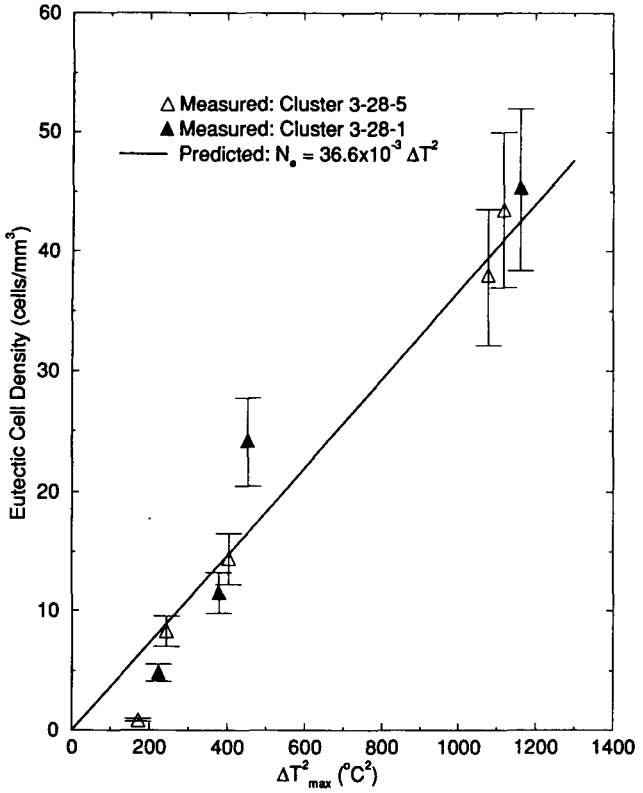

Fig. 5—The relation between cell density and maximum undercooling.

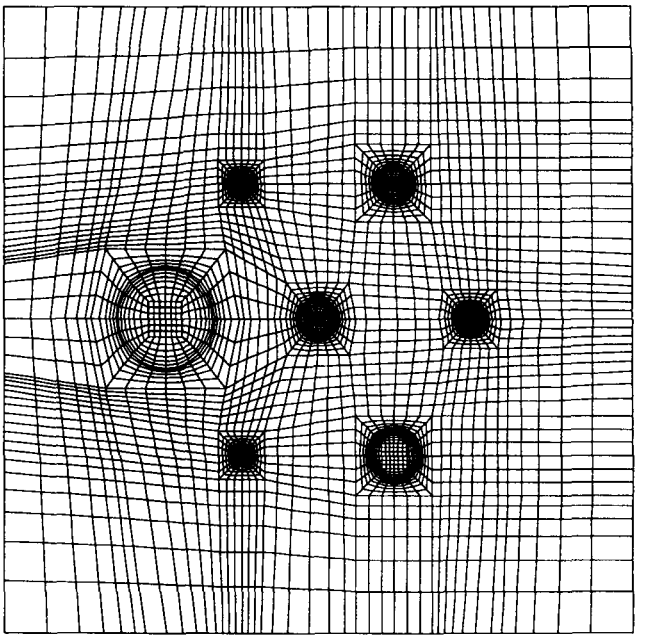

Fig. 7—Two-dimensional finite-element mesh of experimental cluster of castings.

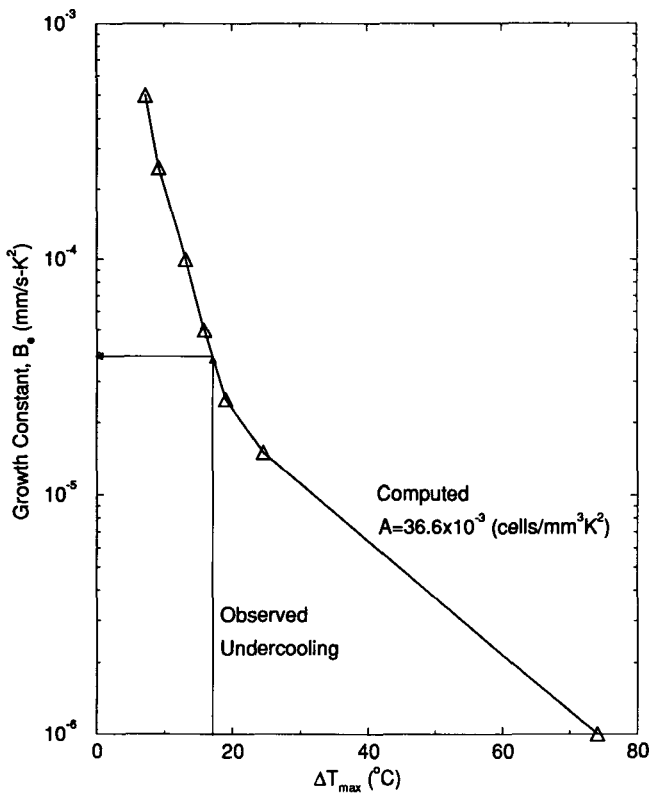

Fig. 6—The relation between undercooling and growth constant for a 25.4-mm-diameter casting.

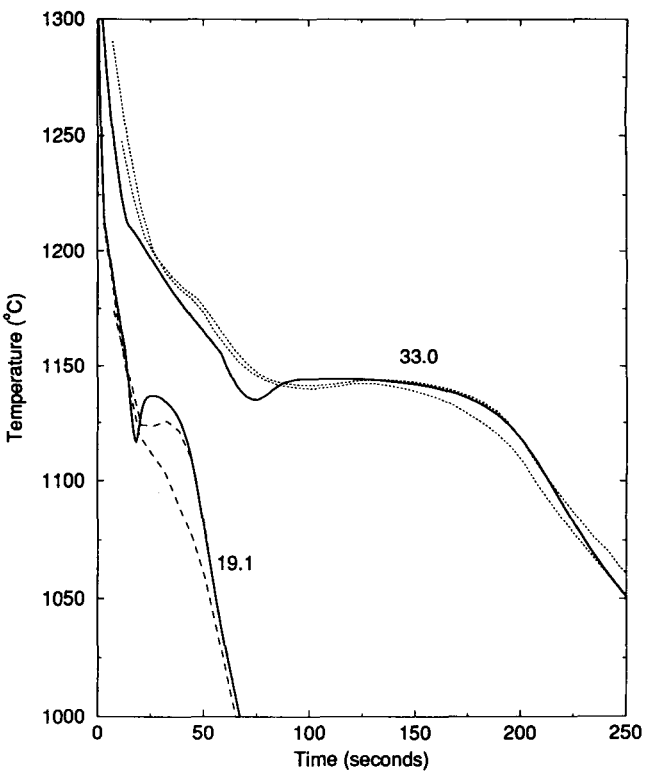

Fig. 8—Predicted temperature curves for cluster casting (solid lines) compared with experimental data from castings 3-28-1 and 3-28-5 (broken lines). Two diameters have been selected for clarity of presentation. The discrepancy for the smallest diameters is the result of time lag in the thermocouple response.

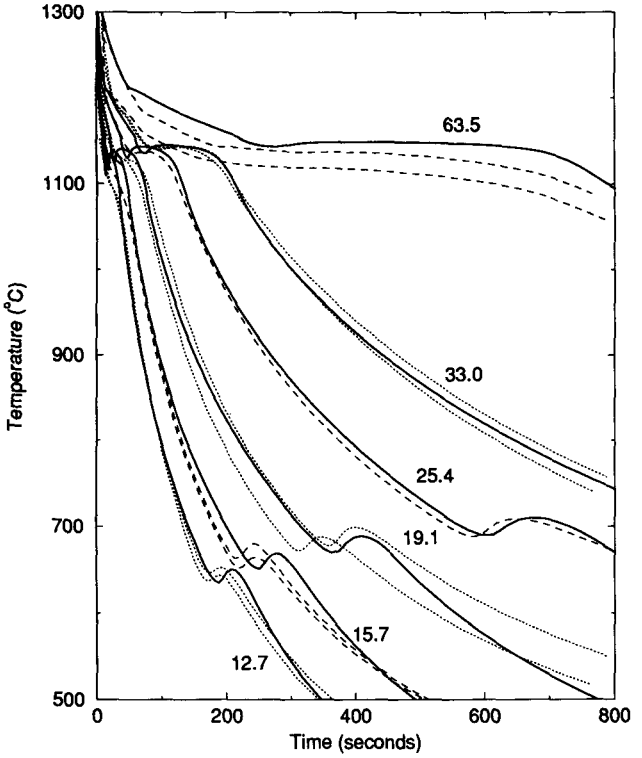

Fig. 9—Predicted temperature curves for cluster casting (solid lines) compared with experimental data from castings 3-28-1 and 3-28-5 (broken lines).

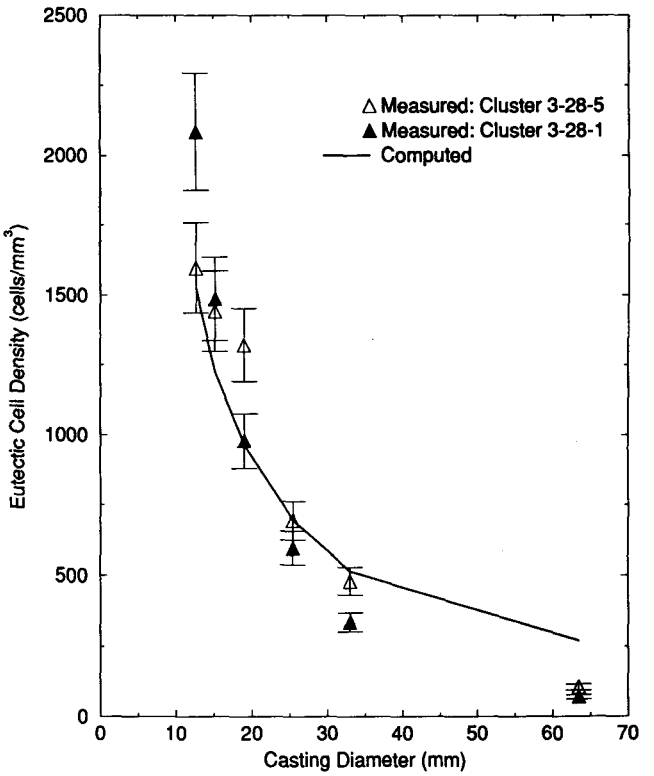

Fig. 10—Measured and predicted eutectic cell density for cluster castings.

in Figure 8 for the small diameter is typical of our experimental results. We attribute this to time lag in the thermocouple data. For the data given in these figures, the impingement factor $\psi = (1 - f_s)^2$ was used. The effects of the various impingement factors will be discussed further in the Section III. Degradation of the bonded sand mold, or air gap formation, are possible explanations for the differences seen in the cooling rate after the eutectoid transformation.

The predicted eutectic cell densities in Figure 10 show excellent agreement with the measured values. The correlation among the full range of diameters confirms the applicability of the growth-rate coefficient for the various process conditions. The small error bars on the largest diameter casting are misleading, because the definition of the grain boundaries decreases with the size of the casting. The cell count for the 63.5-mm casting was very difficult and likely to have a much larger error than 20 pct. Figure 11 shows the measured and predicted maximum eutectic undercoolings. The model is also in good agreement with experimental observations across the full range of casting sizes.

The results shown in Figure 9 used nucleation and growth equations for the eutectoid transformation similar in form to the graphite eutectic kinetic equations (Eqs. [20] and [22]). This model was introduced because the nucleation and growth coefficients of $A_p = 2.0 \times 10^{-3}$ (cells/mm$^3 \cdot$K^2), $n_p = 2.0$, $B_p = 5.0 \times 10^{-7}$ (mm/s), and $m_p = 2.0$ back calculated from the observed undercooling agree very well with the experimental data, as seen in Figure 12. The agreement between the predicted eutectoid undercooling using

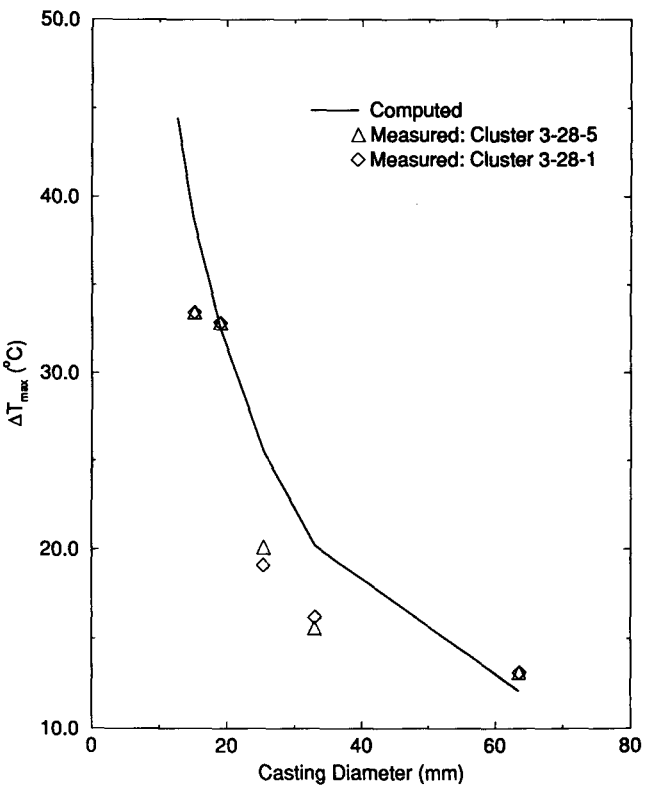

Fig. 11—Measured and predicted maximum eutectic undercooling for cluster castings.

Mehl and Dube pearlite nucleation and growth-rate equations (Eq. [26]) was poor, predicting 25 °C to 75 °C lower than the measured results. The slope of undercooling as a function of casting diameter was not close to the experimental observations.

One of the primary reasons for computing the temperature field for the entire casting was to determine if there was any thermal interaction between the individual cylinders. The temperature field in Figure 13 shows that the neighboring cylinders do influence the individual castings. The overlapping temperature fields did not have a noticeable effect until after the eutectoid transformation and should not affect the predicted microstructure of the castings. The full cluster casting simulation took 205 time-steps and 14 cpu hours on a Sun SPARCstation 1 to complete. An execution profile for a smaller problem revealed that approximately 10 pct of the total cpu time was spent in the microstructure evolution routines.

Mechanical Property Predictions

The main reason for modeling the microstructure development of gray iron is the link it provides to mechanical properties. Gray irons are commonly classified by their minimum tensile strength. For example, a grade 220 gray iron indicates that it has a nominal tensile strength of 220 MPa. Bates[33] investigated the effect of varying alloy additions on the tensile stress to cause failure of gray iron. He determined that ultimate tensile strength in gray iron can be modeled using a Griffith fracture criterion of the form

$$\sigma_f = \frac{K}{\sqrt{c_{\max}}} \qquad [37]$$

where $c_{\max}$ is the maximum graphite flake length and $K = 146.7$ (MPa$\sqrt{\text{m}}$) for an iron containing approximately 2 pct Si and 3.1 to 3.5 pct C. The addition of Si, Mn, Cr, Cu, Ni, Mo, and Sn to gray iron changed the matrix strength (K), but the fracture stress showed the same functional form. The data presented by Bates also showed that the yield strength was approximately 0.8 times the ultimate strength.

In order to use this ultimate tensile strength relation, the maximum graphite flake length must be determined. The graphite flakes in gray iron grow outward in a radial pattern from the eutectic cell center into the remaining eutectic liquid. Assuming the graphite flake does not cross the eutectic cell boundary, the maximum possible flake length would be the largest eutectic cell diameter. Figure 14 shows that the maximum flake length appears to be approximately 75 to 95 pct of the predicted maximum cell diameter. This correlation was used to compute the fracture strength. The hardness was determined from the ultimate tensile strength using[33]

$$\text{BHN} = 0.0284\sigma_f \exp(0.8228 * \text{CE}) \qquad [38]$$

These mechanical property correlations have all been written in terms of microstructural features. Thus, the mechanical property calculations are uncoupled from the heat-flow problem and may be extracted during postprocessing.

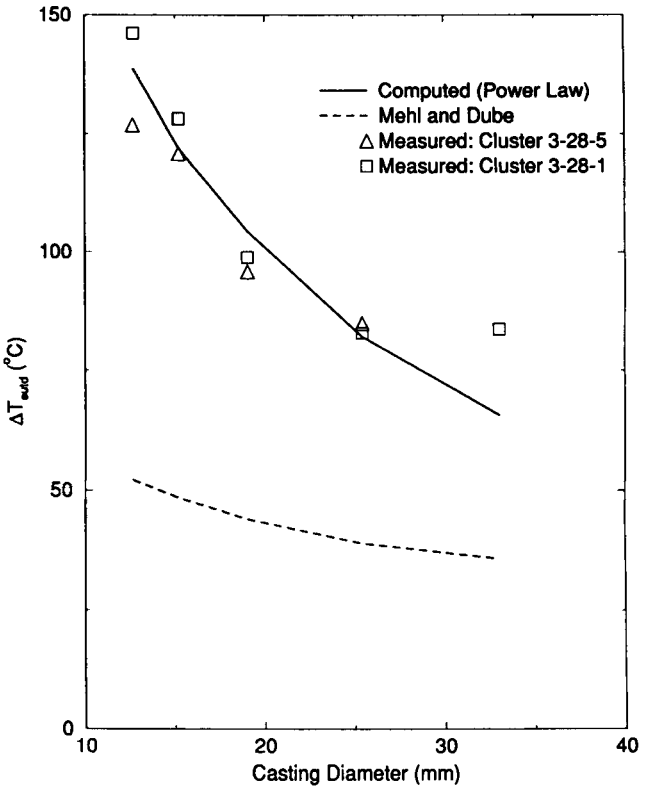

Fig. 12—Measured and predicted maximum eutectoid undercooling for cluster castings.

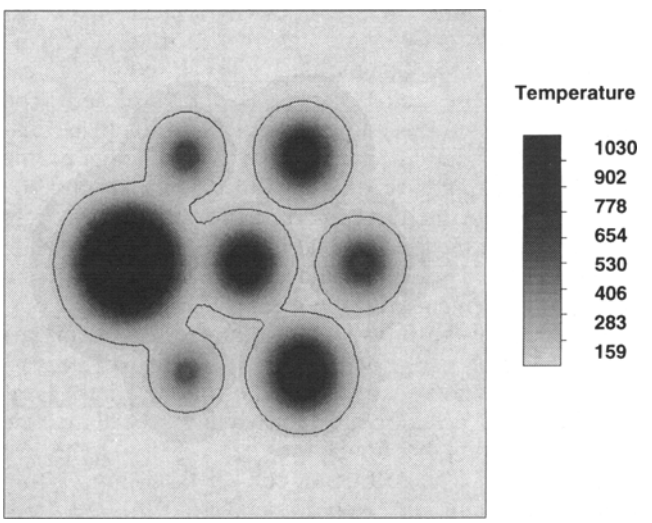

Fig. 13—Temperature distribution in the metal and mold after 300 s. The 100 °C isotherm is also shown to illustrate the overlap of the thermal fields from neighboring cylinders.

To demonstrate the microstructure/mechanical property relationships, and the applicability of the model to more complex shapes, the step casting shown in Figure 15, with ribs of five different thicknesses (25, 18, 12.5, 6, and 3 mm) will be used as an example. The

casting composition was taken to be the same as described in the experiments reported earlier. This casting design was used by Banerjee *et al.*,[34] to test a gray/white iron microstructure model. The two-dimensional finite-element mesh in the iron casting and in the sand mold are illustrated in Figure 15. The mesh had a total of 5804 elements and 5633 nodes. The metal and sand nodes were given an initial temperature of 1300 °C and 35 °C, respectively. The composition, material properties, and kinetic constants used in this example are the same used previously in the cluster casting simulation.

The undercooling ranged from 11 °C in the 25-mm section to 70 °C in the 3-mm section. The maximum undercooling is defined as the point where the cooling rate is zero. If the nucleation-rate constant is very small, and the growth rate is high, no recalescence will occur, and the maximum undercooling will have a recorded value of zero. If this occurred, then maximum undercooling was defined as the temperature where $f_s = 0.52$, the point at which spheres in an fcc arrangement impinge.

The eutectic cell density distribution is shown in Figure 16. The areal density ranged from 330 (cells/cm^2) to 1720 (cells/cm^2), and generally follows the shape of the undercooling contours. The contours are symmetric across the individual bars and clearly show their interaction with the runner base. The 3-mm section has an approximate strength of 280 MPa (40.6 ksi), while the 25-mm section has a strength of 200 MPa (29 ksi). The predicted hardness throughout the casting is shown in Figure 17. The shape is similar to that of the eutectic cell density, as one would expect from the correlation used.

III. DISCUSSION

Sensitivity

One of the greatest benefits of computer simulation is the ability to measure the effect of altering individual variables. In this section, we will investigate the sensitivity of the cooling curve and microstructure to several variables. A 25.4-mm-diameter sand casting will be used as the test case for all of these investigations.

Figure 18 shows the effect of varying the nucleation and growth constants on the computed eutectic undercooling. A series of simulations was performed using the nucleation constants determined by Oldfield[4] (0.91×10^{-3} and 7.12×10^{-3} (cells/mm$^3 \cdot$K^2)) and from this study (36.6×10^{-3} (cells/mm$^3 \cdot$K^2)). The growth relation in Eq. [22] with a power of $2(n_e = 2.0)$ was used for the first three curves, and a constant of $n_e = 1.7$ was used to obtain the last curve. The plot shows that as the

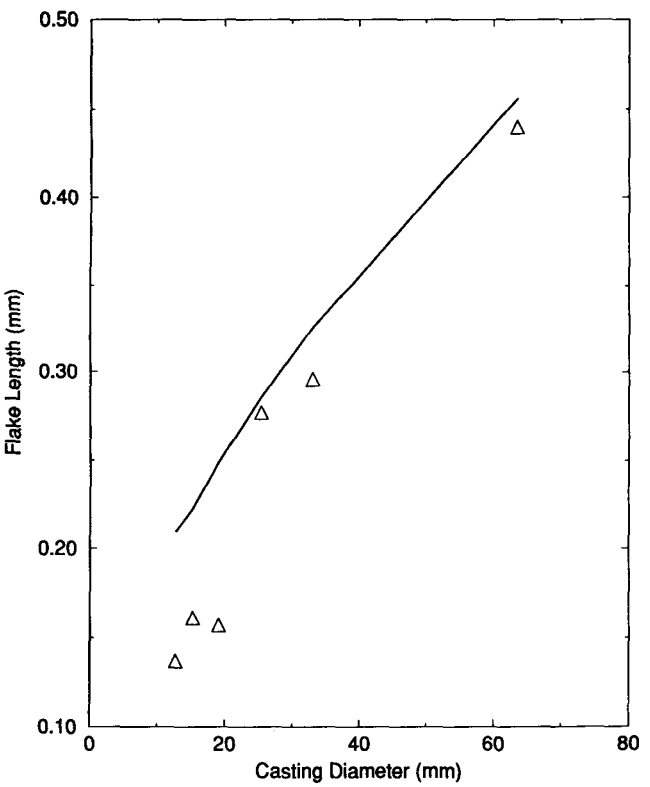

Fig. 14—Comparison of maximum graphite flake length and predicted maximum eutectic cell radius for cylindrical castings.

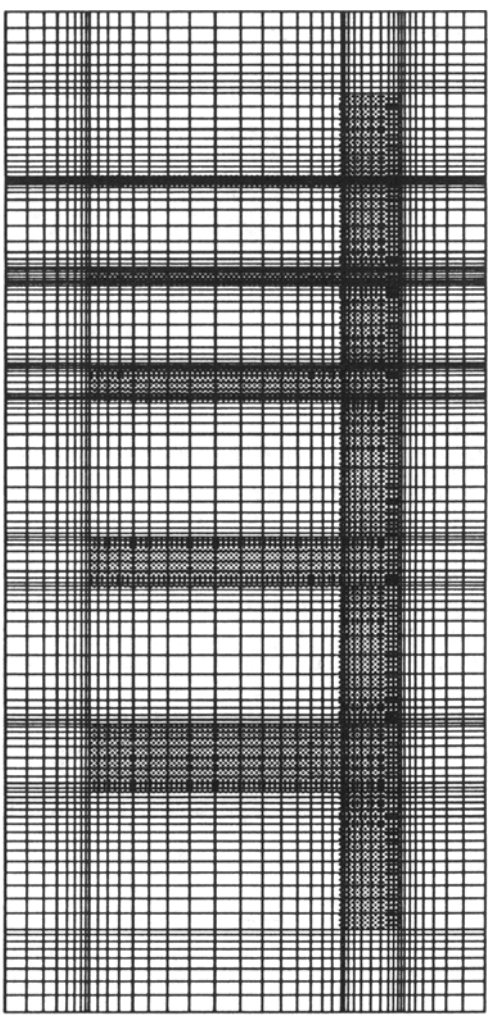

Fig. 15—Finite-element modeling mesh of step casting. The iron is shown as shaded.

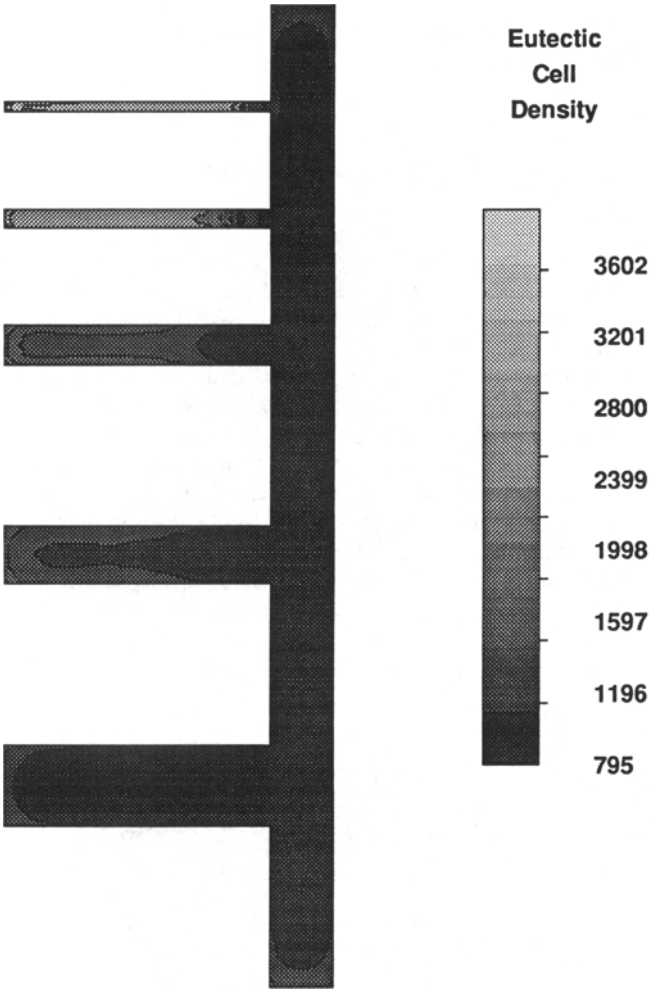

Fig. 16—Eutectic cell density distribution in the step casting.

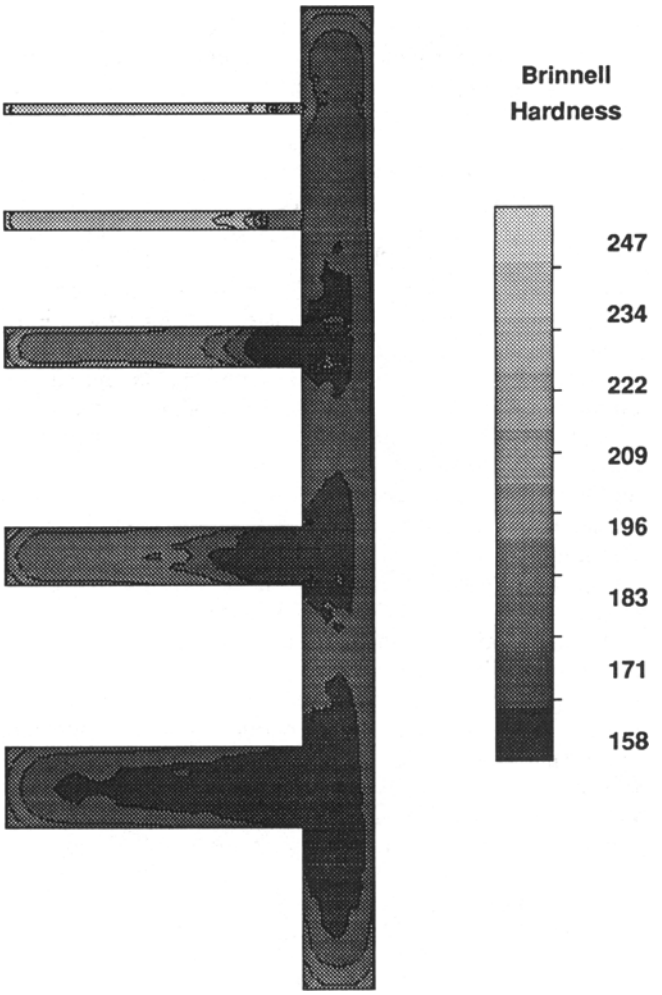

Fig. 17—Hardness distribution in the step casting.

growth-rate constant increases, the importance of varying the nucleation constant decreases. The undercooling varies by only 2 °C when the growth constant is $A_e = 0.384 \times 10^{-1}$, but has a range of 30 °C with a constant of $A_e = 0.384 \times 10^{-5}$ (mm/s). Oldfield mentioned in his work that the growth equation using $n_e = 2.0$ overestimated the undercooling for the small-diameter casting and underestimated for the larger castings. A growth-rate power of $n_e = 1.7$ was proposed to give better correlation. The use of the lower power does reduce the slope of the undercooling/growth-constant curve and is effective in reducing the slope of a cooling rate/undercooling curve. However, the growth equation using $n_e = 2.0$ was able to matching the eutectic undercooling for the full range of casting diameters in our experiments.

Figure 19 and Table V show the effect of varying the form of the impingement coefficient on the cooling curve and cell density distribution parameters. The form of the cell impingement factor has a significant effect on both the distributions and on the cooling curve, particularly near the end of freezing. Note that even when $\psi = 1$, the temperature falls slightly at the end of solidification. This is due to the rapid heat extraction when the surrounding nodes freeze. Banerjee *et al.*[34] noted in their work that the form $(1 - f_s)^3$ gave the best agreement with thermocouple results. This proved to be true in this study also. Unfortunately, the nonlinearity of this term reduces the growth rate at the end of solidification to a point where the volume fraction transformed never reaches 100 pct. This occurred to a lesser extent when using the $(1 - f_s)^2$ form. To deal with this, the solidification was defined to be completed when $f_s = 0.995$ when these forms were used.

In the development of the model for the cell density distribution, a concave-shaped quadratic distribution was assumed. As a test of the sensitivity of the results to the shape of the cell distribution, the convex distribution illustrated in Figure 20 was examined. The resulting form of the distribution is

$$n(\rho_c) = \frac{3N}{2(R - r)^3}(R^2 - 2Rr + 2r\rho_c - \rho_c^2) \quad [39]$$

Table VI shows that both distribution forms give nearly identical results for the maximum eutectic undercooling and cell densities, allowing us to conclude that microstructure evolution is relatively insensitive to the detailed shape of the cell distribution.

The size of the critical nucleus is determined from the Gibbs free energy, solid/liquid interfacial energy,

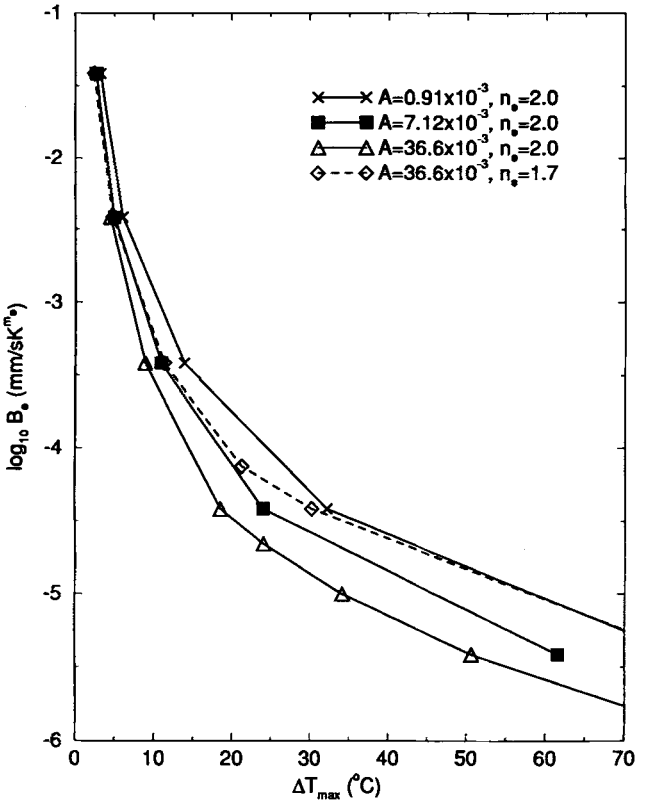

Fig. 18—Effect of varying growth- and nucleation-rate constants on the eutectic undercooling.

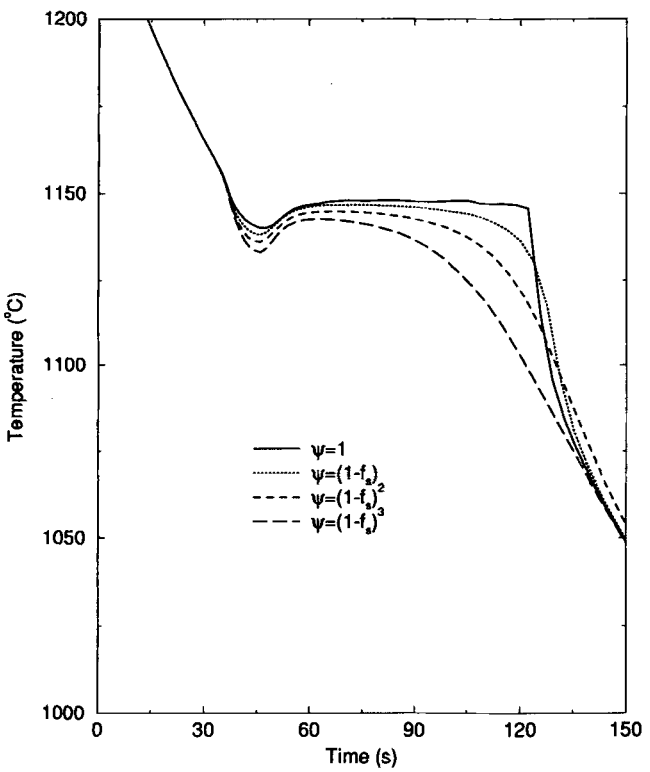

Fig. 19—Effect of varying the impingement coefficient on the cooling curve of a 25.4-mm-diameter casting. Note that even when $\psi = 1$, the temperature falls slightly at the end of solidification. This is due to the rapid heat extraction when the surrounding nodes freeze.

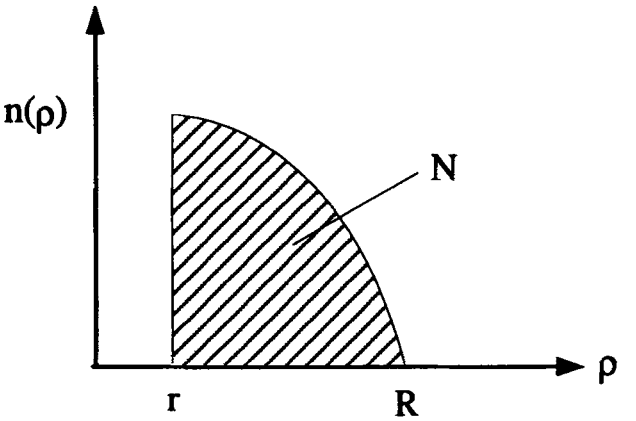

Fig. 20—Quadratic Cell Distribution with Convex Shape.

undercooling, and the wetting angle. However, the size chosen for the initial particles is relatively unimportant in determining the final cell density. Using initial nucleus sizes ranging from 1.0×10^{-5} to 0.01 mm produced no significant changes in either computed undercooling, cell density, or solidification time. Larger initial nucleus sizes are physically unrealistic.

The formulation used in the Fe-Fe_3C development could be greatly improved by further study of the interaction of gray and white iron transformations below the metastable eutectic temperature. The present method stops the growth of the graphite eutectic and starts Fe_3C nucleation and growth when the temperature falls below the Fe-Fe_3C equilibrium temperature. This method was a first attempt and needs further refinement. Competitive growth between the two structures would represent a more realistic approach.

Another area that needs further investigation is the kinetic expressions for the eutectoid transformation. The exponential nucleation and growth relations introduced by Mehl and Dube[21] predicted substantially lower undercoolings than we observed in our experiments. Although a power law relation was able to give good agreement for our experiments, the limited range of compositions examined cautions against assuming the results are generally applicable. It would be very helpful if the information from TTT or CCT diagrams could be implemented into the microstructure model, as Zou and Tseng[35] have presented. This would take advantage of a large data base of information, as well as extending the model to microstructure development in a heat-treatment cycle.

The mechanical property relations used in this study are just a first step in providing a usable design tool. Implementing a data base including the effects of various alloy compositions on the mechanical properties is the next logical step.

IV. CONCLUSIONS

A microstructure model has been developed to predict the evolution of microstructure during solidification of cast irons in foundry casting. Expressions for nucleation and growth of gray iron have been incorporated within a commercial finite-element code for transient heat-flow

Table V. Predicted Results of Varying the Impingement Coefficient on the Cooling Curve of a 25.4-mm-Diameter Casting

Impingement Coefficient	Maximum Eutectic Undercooling (°C)	Eutectic Cell Density (cells/mm^3)	Eutectic Cell Density (cells/cm^2)	Minimum Radius (mm)	Maximum Radius (mm)	Final Solidification Time (s)
None	14.9	8.1	470	0.268	0.349	126
$(1 - f_s)$	16.9	10.4	560	0.248	0.316	132
$(1 - f_s)^2$	18.9	13.2	650	0.229	0.296	172
$(1 - f_s)^3$	21.8	17.4	790	0.206	0.274	343

Table VI. Predicted Results of Varying Cell Density Distribution on the Cooling Curve of a 25.4-mm-Diameter Casting

Cell Distribution	Maximum Eutectic Undercooling (°C)	Eutectic Cell Density (cells/mm^3)	Eutectic Cell Density (cells/cm^2)	Minimum Radius (mm)	Maximum Radius (mm)	Final Solidification Time (s)
Concave	18.9	13.2	650	0.228	0.296	172
Convex	18.6	12.6	640	0.222	0.281	171

Table VII. Temperature-Dependent Material Properties for Resin-Bonded Sand and Iron

Temperature (°C)	Sand Specific Heat (J/g · K)	Iron Thermal Conductivity (W/mm · K)	Sand Thermal Conductivity (W/mm · K)
0	0.7113	6.087×10^{-4}	6.686×10^{-2}
100	0.8577	6.401×10^{-4}	5.950×10^{-2}
200	0.9665	6.629×10^{-4}	5.560×10^{-2}
300	1.0334	6.925×10^{-4}	5.030×10^{-2}
400	1.0962	7.186×10^{-4}	4.520×10^{-2}
500	1.1380	7.777×10^{-4}	4.000×10^{-2}
600	1.1548	8.301×10^{-4}	3.510×10^{-2}
700	1.1715	9.123×10^{-4}	3.301×10^{-2}
800	1.1757	1.010×10^{-4}	2.972×10^{-2}
900	1.1799	1.122×10^{-4}	2.600×10^{-2}
1000	1.1883	1.226×10^{-3}	2.227×10^{-2}
1100		1.383×10^{-3}	
1120.6		1.413×10^{-3}	
1121.1		1.436×10^{-3}	
1137.8		1.451×10^{-3}	
1150		1.466×10^{-3}	
1200		1.563×10^{-3}	8.908×10^{-2}
1215.6	1.1883	1.585×10^{-3}	
1300	1.1924	1.660×10^{-3}	
1350	1.1966	1.810×10^{-3}	
1430	1.1966	1.973×10^{-3}	8.908×10^{-2}

calculation. The kinetic equations are solved in terms of a cell density distribution function. This has the advantages of reducing the number of variables needed to describe the microstructure, simplifying error control, and providing a straightforward means of comparing the computed results with experimentally observed microstructures. Features predicted include eutectic cell size, prevalence of gray *vs* white iron, graphite morphology, pearlite and ferrite grain size, and pearlite lamellar spacing. Predictions of the model are in good agreement with the temperature and metallographic data derived from our experiments. Predicted strength and fatigue properties are consistent with published data but have not been critically tested. The main results and conclusions from this work are summarized below.

1. The temperature recovery method coupled with a statistical representation of the microstructural features has been shown to be a numerically robust approach to implement solidification and microstructure modeling in a finite-element method code.
2. The cell density and temperature history are insensitive to the assumption critical nucleus size, as well as to the details of the assumed shape of the cell density distribution.
3. Calculation of microstructural features increases the computing time of the calculations, but not to an excessive extent.
4. Nucleation and growth coefficients $A_e = 0.03663$ (cells/mm^3 · K^2) and $B_e = 3.84 \times 10^{-5}$ (mm/s) were determined for the experimental casting in this study.

Table VIII. Latent Heat for Iron Phase Transformations

Microstructure	Latent Heat (J/g · K)
Primary austenite	263[37]
Austenite-graphite eutectic	233[37]
Iron-carbide eutectic	213[37]
Pearlite	85.8[38]
Ferrite	16.3[39]

5. The predicted maximum eutectic cell radius has been seen to be proportional to the measured maximum graphite flake length over a range of section sizes.

APPENDIX

Thermophysical properties

The density of the sand was taken to be a constant, 1.442×10^{-3} g/mm^3. The density of the iron was also taken to be constant, 7.23×10^{-3} g/mm^3, and the specific heat was taken as 0.91 J/g · K. The remaining properties were temperature dependent and are listed in Tables VII and VIII. Piecewise linear interpolation was used between neighboring points in the tables.

ACKNOWLEDGMENTS

The authors gratefully acknowledge the support of Caterpillar Inc. The assistance and guidance of Julia Coffman and John Graebel in conducting the experimental program, and the metallography laboratory at Caterpillar Technical Center were invaluable.

REFERENCES

1. J.W. Wiese and J.A. Dantzig: *Metall. Trans. A*, 1990, vol. 21A, pp. 489-97.
2. J.A. Dantzig and J.W. Wiese: *Adv. Manufac. Proc.*, 1986, vol. 1, pp. 437-54.
3. K. Kubo and R.D. Pehlke: *Metall. Trans. B*, 1985, vol. 16B, pp. 359-66.
4. W. Oldfield: *Trans. ASM*, 1966, vol. 59, 945-60.
5. A. Hellawell: in *Solidification Processing*, Institute of Metals, London, 1977, pp. 161-68.
6. M. Rappaz: *Int. Mater. Rev.*, 1989, vol. 34, pp. 93-123.
7. M. Rappaz and D. Stefanescu: in *Solidification Processing of Eutectic Alloys*, D.M. Stefanescu, G.J. Abbaschian, and R.J. Bayuzick, eds., TMS, Warrendale, PA, 1988, pp. 133-51.
8. D. Stefanescu and D. Bandyopadhyay: in *Casting of Near Net Shape Products*, Y. Sahai, J.E. Battles, R.S. Carbonara, and C.E. Mobley, eds., TMS, Warrendale, PA, pp. 153-65.
9. W.A. Johnson and R.F. Mehl: *Reaction Kinetics in Processes of Nucleation and Growth*, 1939, AIME Technical Publication No. 1089, pp. 1-27.
10. M. Avrami: *J. Chem. Phys.*, 1940, vol. 8, pp. 212-24.
11. C. Price: *Acta Metall.*, 1987, vol. 35, pp. 1377-90.
12. T. Clyne and W. Kurz: *Metall. Trans. A*, 1981, vol. 12A, pp. 965-71.
13. R.W. Heine: *AFS Trans.*, 1986, vol. 94, pp. 391-402.
14. D. Glover, C.E. Bates, and R. Monroe: *AFS Trans.*, 1982, vol. 90, pp. 745-57.
15. D. Turnbull and J.C. Fisher: *J. Chem. Phys.*, 1949, vol. 17, p. 71.
16. R. Elliott: *Eutectic Solidification Processing*, Butterworths and Co., Ltd., London, 1983.
17. J.-T. Thorgrimsson, H. Fredriksson, and I. Svensson: in *Solidification Processing*, Institute of Metals, London, 1987, pp. 83-86.
18. P. Magnin and W. Kurz: *Acta Metall.*, 1987, vol. 35, pp. 1119-28.
19. M. Hillert and V.V. Subba Rao: in *The Solidification of Metals*, The Iron and Steel Institute, London, 1967, pp. 205-12.
20. G. Ruff and J. Wallace: *AFS Trans.*, 1976, vol. 84, pp. 705-28.
21. R. Mehl and A. Dube: in *Phase Transformations in Solids*, R. Smoluchowski, J.E. Mayer, and W.A. Weyl, eds., John Wiley and Sons, Inc., New York, NY, 1951.
22. D.M. Stefanescu and C. Kanetkar: in *Computer Simulation of Microstructural Evolution*, D.J. Srolovitz, ed., Warrendale, PA, 1986, pp. 171-88.
23. W. Press, B. Flannery, S. Teukolsky, and W. Vetterling: *Numerical Recipes*. Cambridge University Press, Cambridge, United Kingdom, 1986.
24. T. Tszeng, Y. Im, and S. Kobayashi: *Int. J. Mach. Tools Manufac.*, 1989, vol. 29, pp. 107-200.
25. M. Engelman: *FIDAP Theoretical Manual*, Fluid Dynamics International, Evanston, IL, 1990.
26. W. Oldfield: *BCIRA J.*, 1961, vol. 9, pp. 506-18.
27. W. Oldfield: *BCIRA J.*, 1960, vol. 8, pp. 177-92.
28. M. Horsfall: *BCIRA J.*, 1982, vol. 30, pp. 134-39.
29. M. Horsfall: BCIRA Technical Report, 1981.
30. H.D. Merchant: *Foundry*, 1963, vol. 91, pp. 59-65.
31. *Metals Handbook*, 4th ed. E.E. Underwood, ed., ASM, Metals Park, OH, 1985, pp. 123-34.
32. J.V. Dawson and W. Oldfield: *BCIRA J.*, 1960, vol. 8, pp. 221-31.
33. C.E. Bates: *AFS Trans.*, 1986, vol. 94, pp. 889-912.
34. D.K. Banerjee, G. Upadhya, and D.M. Stefanescu: in *F. Weinberg Int. Symp. on Solidification Processing*, J.E. Lait and I.V. Samarasekera, eds., Pergamon Press, Inc., New York, NY, 1990, pp. 319-32.
35. J. Zou and A.A. Tseng: *Metall. Trans. A*, 1992, vol. 23A, pp. 457-67.
36. R.D. Pehlke, A. Jeyarajan, and H. Wada: *Summary of Thermal Properties for Casting Alloys and Mold Materials NITS-PB83-211003*, University of Michigan, Ann Arbor, 1982.
37. D.M. Stefanescu: in *The Physical Metallurgy of Cast Iron*, H. Fredriksson and M. Hillert, eds., North-Holland, Amsterdam, 1984.
38. C. Zener: *Trans. AIME*, 1946, vol. 167, pp. 550-67.
39. L.S. Darken and R.P. Smith: *Ind. Eng. Chem.*, 1951, vol. 43, pp. 1815-19.